ARTICLE TYPE www.rsc.org/xxxxxx | XXXXXXXX

Towards homonuclear *J* solid-state NMR correlation experiments for half-integer quadrupolar nuclei: experimental and simulated ^{11}B MAS spin-echo dephasing and calculated $^{2}J_{BB}$ coupling constants for lithium diborate

Nathan S. Barrow,[a] Jonathan R. Yates,[b] Steven A. Feller,[c] Diane Holland,[a] Sharon E. Ashbrook,[d] Paul Hodgkinson[e] and Steven P. Brown*[a]

Received (in XXX, XXX) Xth XXXXXXXXX 201X, Accepted Xth XXXXXXXXX 201X
First published on the web Xth XXXXXXXXX 201X
DOI: 10.1039/b000000x

Magic-angle spinning (MAS) NMR spin-echo dephasing is systematically investigated for the spin $I = 3/2$ ^{11}B nucleus in lithium diborate, $Li_2O.2B_2O_3$. A clear dependence on the quadrupolar frequency ($\omega_Q^{PAS}/2\pi = 3C_Q/[4I(2I-1)]$) is observed: the B3 (larger C_Q) site dephases more slowly than the B4 site at all investigated MAS frequencies (5 to 20 kHz) at 14.1 T. Increasing the MAS frequency leads to markedly slower dephasing for the B3 site, while there is a much less evident effect for the B4 site. Considering samples at 5, 25, 80 (natural abundance) and 100 % ^{11}B isotopic abundance, dephasing becomes faster for both sites as the ^{11}B isotopic abundance increases. The experimental behaviour is rationalised using density matrix simulations for two and three dipolar-coupled ^{11}B nuclei. The experimentally observed slower dephasing for the larger C_Q (B3) site is reproduced in all simulations and is explained by the reintroduction of the dipolar coupling by the so-called "spontaneous quadrupolar-driven recoupling mechanism" having a different dependence on the MAS frequency for different quadrupolar frequencies. Specifically, isolated spin-pair simulations show that the spontaneous quadrupolar-driven recoupling mechanism is most efficient when the quadrupolar frequency is equal to twice the MAS frequency. While for isolated spin-pair simulations, increasing the MAS frequency leads to faster dephasing, agreement with experiment is observed for three-spin simulations which additionally include the homogeneous nature of the homonuclear dipolar coupling network. First-principles calculations, using the GIPAW approach, of the $^{2}J_{11B\text{-}11B}$ couplings in lithium diborate, metaborate and triborate are presented: a clear trend is revealed whereby the $^{2}J_{11B\text{-}11B}$ couplings increase with increasing B-O-B bond angle and B-B distance. However, the calculated $^{2}J_{11B\text{-}11B}$ couplings are small (0.95, 1.20 and 2.65 Hz in lithium diborate), thus explaining why no zero crossing due to *J* modulation is observed experimentally, even for the sample at 25 % ^{11}B where significant spin-echo intensity remains out to durations of ~200 ms.

Introduction

Solid-state magic-angle-spinning (MAS) NMR experiments, that use *J* couplings to establish two-dimensional through-bond homonuclear correlations, e.g., TOBSY,[1-2] refocused INADEQUATE,[3-5] and double-quantum (DQ) filtered- or sensitive absorptive refocused (SAR)- COSY[6-7] are being increasingly widely utilised for spin $I = 1/2$ nuclei, e.g., ^{13}C, ^{15}N, ^{19}F, ^{29}Si, and ^{31}P. Spectra have been presented for a variety of organic and inorganic systems, e.g., celluloses,[3,8] phosphates,[9-10] a C_{60} fullerene,[11] molecules exhibiting NH…N hydrogen bonding,[12-13] a surfactant-templated silicate layers,[14] and a fluorinated hydroxy-silicate.[15]

While approximately two-thirds of all NMR-active nuclei are quadrupolar ($I \geq 1$), there are very few examples of solid-state NMR experiments that utilise, observe or probe *J* couplings between two half-integer quadrupolar nuclei.[16] Specifically, splittings due to $^{1}J_{11B\text{-}11B}$, $^{1}J_{11B\text{-}14N}$ and $^{1}J_{55Mn\text{-}55Mn}$ couplings have been observed in MQMAS spectra,[17] while heteronuclear ^{27}Al-^{17}O spectra have been presented for experiments that rely on $^{1}J_{17O\text{-}27Al}$ couplings for coherence transfer,[18-19] and the $^{2}J_{17O\text{-}17O}$ coupling in ^{17}O-labelled glycine.HCl has been determined from MAS spin-echo experiments.[20] To the best of our knowledge, there are no published examples of two-dimensional MAS homonuclear *J* correlation experiments for quadrupolar nuclei. It is to be noted, however, that through-space dipolar couplings between quadrupolar nuclei have been used to establish two-dimensional homonuclear correlations, e.g., spin-diffusion exchange experiments or double-quantum or higher multiple-quantum (MQ) experiments.[21-22]

This paper sets out to determine whether *J* homonuclear correlation experiments are feasible for half-integer quadrupolar nuclei by investigating, both experimentally and in simulation, spin-echo dephasing for the half-integer

quadrupolar nucleus, ^{11}B (I = 3/2), in the model polycrystalline compound, lithium diborate, $Li_2O.2B_2O_3$. ^{11}B is an important nucleus for solid-state NMR applications to materials science with MAS as well as high-resolution methods such dynamic-angle spinning (DAS), double rotation (DOR) and MQ MAS experiments and 2D exchange and heteronuclear experiments having been performed for, e.g., vitreous B_2O_3,[23-26] borate and borosilicate glasses,[27-30] including potential hosts for nuclear waste immobilisation,[31-32] BN and BCN ceramics and precursors,[33-35] organoboron compounds[36-38] and boranes of interest for hydrogen storage.[39]

Edén and Frydman have previously shown how the interplay of dipolar and quadrupolar interactions affect ^{11}B lineshapes[40] and two-dimensional ^{11}B-^{11}B spin-diffusion experiments.[41] For two dipolar-coupled spin I = 1/2 nuclei, the well-known rotational-resonance phenomena arise from the non-commutation (and hence incomplete refocusing under MAS) of the homonuclear dipolar coupling and the chemical shift anisotropy (CSA).[42-43] In analogy to this, Edén and Frydman have introduced the term "spontaneous quadrupolar-driven recoupling" for the incomplete removal by MAS of the homonuclear dipolar coupling between two quadrupolar (I > 1/2) nuclei that arises from the non-commutation of the dipolar and quadrupolar couplings. This analysis builds upon work by Gan and Robyr[44] and Facey et al.[45] for the case of a dipolar coupling between two ^{2}H (spin I = 1) nuclei.

Specifically, Edén and Frydman have shown by simulation and experiment that the central-transition linewidth can depend on the MAS frequency, and can even be observed to increase as the MAS frequency is increased (see Fig. 3 of Ref.[40] for ^{7}Li (spin I = 3/2) NMR of Li_2SO_4, $LiOH.H_2O$ and $Li_2C_2O_4$ and ^{79}Br (spin I = 3/2) NMR of KBr). Facey et al. have shown that line broadening is also observed in ^{2}H (spin I = 1) MAS NMR spectra of strongly dipolar coupled deuterium pairs in transition metal dihydrides.[45] (Note that for the case of an isolated half-integer quadrupolar nucleus experiencing only the quadrupolar interaction, the linewidth is independent of the MAS frequency.) Defining the quadrupolar frequency[46] as $\omega_Q^{PAS} = 3\pi C_Q/[2I(2I-1)]$, i.e., $\omega_Q^{PAS}/2\pi = C_Q/4$ for I = 3/2, maximum experimental line broadening in the ^{7}Li MAS spectra presented in Fig. 3 of Ref.[40] is observed when $\omega_Q^{PAS}/\omega_r \sim 2$. (Note that Edén and Frydman use a parameterisation in terms of $\chi_Q = 2\pi C_Q/[2I(2I-1)]$, i.e., $\chi_Q = (2/3)\ \omega_Q^{PAS}$, hence Ref.[40] states that the maximum line broadening is observed when χ_Q/ω_r = 1.2-1.3.)

This lineshape broadening due to quadrupolar-driven recoupling is most pronounced for two coupled nuclei with identical isotropic chemical shifts (e.g., see Fig. 6 of Ref.[40]). This is analogous to n = 0 rotational-resonance as observed in spin I = 1/2 MAS experiments for the case where two dipolar-coupled nuclei have the same isotropic chemical shifts.[47-50] The simulations in Ref.[40] also show a dependence on the relative orientation of the three tensors (the quadrupolar tensors for the two spins and the internuclear vector that defines the dipolar coupling), with an enhanced effect for a mutually perpendicular arrangement. Note that a quadrupolar-driven recoupling effect is observed for the case of parallel quadrupolar tensors (that are not colinear with the dipolar coupling); this is different to the spin I = 1/2 n=0 rotational resonance effect, where no effect is observed if the two CSA tensors are parallel.[42-43]

In this study, the effect of ^{11}B-^{11}B dipolar couplings on ^{11}B spin-echo dephasing is investigated using samples of polycrystalline lithium diborate, $Li_2O.2B_2O_3$, with three different degrees of ^{11}B depletion/enrichment: 5%, 25% and 100%. (At natural abundance, 80% of boron nuclei are ^{11}B, with the remainder (20%) being ^{10}B.). The experimental results are complemented by two- and three-spin density-matrix simulations and first-principles calculations of the $^2J_{BB}$ couplings.

Experimental and computational details

Synthesis of lithium diborate samples

Polycrystalline lithium diborate, $Li_2O.2B_2O_3$, at natural abundance in ^{11}B was prepared by mixing together 4.369 g of lithium carbonate (Alfa Aesar #013418, 99 %) and 8.233 g of boron oxide (Alfa Aesar #089964, 99.98 %). After agitating the mixture to ensure homogeneity, the reactants were transferred to a platinum-rhodium crucible and placed in a normal-atmosphere electric furnace at 100 °C. The temperature was ramped at 5 °C/min for 3 h to 1000 °C. This temperature was chosen as it is above the congruent melting temperature of lithium diborate (917 ± 2 °C).[51] After 20 min at 1000 °C, the melt was poured onto a room-temperature steel plate.

$$Li_2CO_3 + 2B_2O_3 \rightarrow Li_2O.2B_2O_3 + CO_2$$

Polycrystalline lithium diborate samples with varying degrees of ^{11}B depletion/enrichment were prepared by mixing lithium carbonate (Sigma-Aldrich #255823, 99 %), boric-^{10}B acid (Sigma-Aldrich #426156, 99%) and boric-^{11}B acid (EaglePicher #Bl-EV-95-10, 99.3%) in the correct stoichiometric ratio: for 100% ^{11}B, 3.651 g $^{11}B(OH)_3$ & 1.087 g Li_2CO_3; for 25% ^{11}B, 1.486 g $^{11}B(OH)_3$, 4.388 g $^{10}B(OH)_3$ & 1.771 g Li_2CO_3; for 5% ^{11}B, 0.299 g $^{11}B(OH)_3$, 5.584 g $^{10}B(OH)_3$ & 1.779 g Li_2CO_3. The reagents were thoroughly mixed in a gold (5%)-platinium crucible and placed in a normal-atmosphere electric furnace at 1000 °C. After 15 min, the crucible was removed and weight-loss measurements were performed to check that the expected reaction had occurred. The crucible was returned to the furnace at the higher temperature of 1100 °C to decrease the viscosity of the melt before pouring. After 5 min, the melt was poured onto a room-temperature steel plate and allowed to crystallise.

$$Li_2CO_3 + 4B(OH)_3 \rightarrow Li_2O.2B_2O_3 + CO_2 + 6H_2O$$

For all samples, crystallinity and phase purity were checked by Raman spectroscopy and powder X-ray diffraction (see Fig. S1 in the ESI).

Solid-state NMR experiments

^{11}B MAS experiments were performed on a Bruker Avance II+ spectrometer at a Larmor frequency of 192.53 MHz (corresponding to a ^{1}H Larmor frequency of 599.98 MHz),

using a 3.2 mm probe. ^{11}B chemical shifts were referenced to the primary reference, boron trifluoride diethyl etherate, $BF_2.Et_2O$,[52] using sodium borohydride, $NaBH_4$, (–42.06 ppm) as a secondary reference.[53]

Spin-echo experiments were performed using a 90° – τ/2 – 180° – τ/2 – t_{acq} pulse sequence, where the τ/2 durations are an integer number of rotor periods. Except where otherwise stated, the central-transition selective 90° and 180° pulses were of duration 12.5 and 25 μs, respectively. The selection of the +1 to −1 coherence-transfer pathway was achieved by a 16-step phase cycle that selected $\Delta p = +1$ (4 steps) and $\Delta p = \pm 2$ (4 steps) on the 90° and 180° pulses, respectively. The application of the pulse sequence was preceded by a pulse comb, consisting of thirty-three 90° pulses of duration 2.1 μs separated by free-precession periods of 11 μs, followed by a relaxation delay of 32 s.

For all spin-echo experiments, the magic angle was set by maximising the number of spinning sidebands in a ^{79}Br spectrum of KBr. This enables the angle to be set to within better than 0.1º of the magic angle.[54] While more accurate setting of the magic angle can be achieved, that is important for, e.g., satellite-transition (ST) MAS experiments[55-56] or the observation of very-narrow ^{13}C CP MAS resonances,[57] this is sufficient to avoid noticeable effects on spin-echo dephasing times due to changes in satellite transition rotational resonance conditions[58] or the introduction of residual dipolar couplings.[59-60]

The spin-echo intensities were obtained by taking, after Fourier transformation, integrals over the chemical shift range: 20 to 6 ppm for the B3 site and 6 to −3 ppm for the B4 site. Integration is necessary to ensure that, for the case of modulation by a *J* coupling, only in-phase lineshapes with a cosine spin-echo (τ) modulation are considered, i.e., there is no contribution from anti-phase lineshapes which have a sine spin-echo (τ) modulation. The first recorded integrated spin-echo intensity, corresponding to one rotor period, was normalised to one. Errors on the fitted parameters are determined from the covariance matrix, as described in Ref. [61].

Density-matrix simulations

Spin-echo dephasing curves were simulated using pNMRsim.[62] Evolution under the combined effect of the dipolar coupling and the quadrupolar coupling (with zero asymmetry parameter) during the rotor-synchronised spin-echo periods was simulated explicitly in the density-matrix formalism using the Liouville-von Neumann equation,[63-66] starting with an initial state of *x* magnetisation on the two-coupled spins. (The ESI shows that second-order quadrupolar-dipolar and quadrupolar-CSA cross terms[17,67-68] are small, and they are thus not included in the simulations.) Evolution during the 180° pulse was not explicitly considered, rather perfect $+p$ to $-p$ coherence transfer was simulated by simple exchange of density matrix elements. This ensures that the block diagonal nature of the density matrix is maintained throughout, allowing time-efficient simulation.[63,69] The resulting signal was read out by using a detection operator corresponding to central-transition single-quantum coherence ($p = -1$). Powder averaging was performed over a total of 2400 different values of the α, β and γ angles according to the ZCW scheme.[70-72] The details of the approach used for the efficient simulation of spin-echo signals, together with a sample input file, are presented in the ESI.

First-principles calculation of $^2J_{BB}$ couplings

First-principles calculations were performed using the CASTEP software package, which implements density-functional theory using a plane-wave basis set and the pseudopotential approach, and is thus applicable to periodic systems. Magnetic resonance parameters were calculated using the GIPAW[73-76] approach which enables the calculation of chemical shifts, electric field gradients and *J* couplings. Calculations were performed using the experimental X-ray diffraction crystal structure of lithium diborate (ICSD reference code: 65930), as well as geometry optimised (CASTEP) structures (both at X-ray diffraction and optimised lattice parameters). The resulting NMR parameters were found to be rather similar – for example, the maximum change in the calculated isotropic *J* coupling on performing a full variable cell optimisation was 0.2 Hz for $^2J_{11\text{-}11B}$ and 1 Hz for $^1J_{11B\text{-}17O}$. Calculated values reported in this article used the experimental X-ray diffraction crystal structure. All calculations used the Perdew-Burke-Ernzerhof (PBE) implementation of the generalized gradient approximation to the exchange-correlation functional.[77] Geometry optimisation used ultra-soft pseudopotentials,[78] and a plane-wave cut-off of 600 eV and a maximum *k*-point spacing of 0.1 $Å^{-1}$. Calculations of all NMR parameters used Trouiller-Martins norm-conserving pseudopotentials[79] with a plane-wave cut-off of 1000 eV and a *k*-point spacing of 0.1 $Å^{-1}$. The *J* couplings are computed by considering one nucleus as a perturbation; this breaks translational symmetry and for small primitive cells it can be necessary to multiply the size of the original crystal unit cell until the values of the couplings are converged. It was found that the primitive cell of lithium diborate was of sufficient size to give well converged *J* coupling without needing to consider such a supercell. The calculation time for the *J* couplings was 4 hours on a dual-quad core Intel E5540 (2.53 GHz) at the Oxford Supercomputer Centre.

Experimental results

^{11}B-^{11}B dipolar couplings in lithium diborate

As shown in Fig. 1, crystalline lithium diborate exhibits superstructural diborate units.[80] Each diborate unit consists of two three-coordinated boron atoms and two four-coordinated boron atoms. Boron−boron distances are presented in Table 1, which also lists the corresponding homonuclear ^{11}B-^{11}B dipolar coupling constants, d_{jk},

$$d_{jk} = -\frac{\mu_0 \gamma_{11B}^2 \hbar}{4\pi r_{jk}^3} \Big/ 2\pi \qquad (1)$$

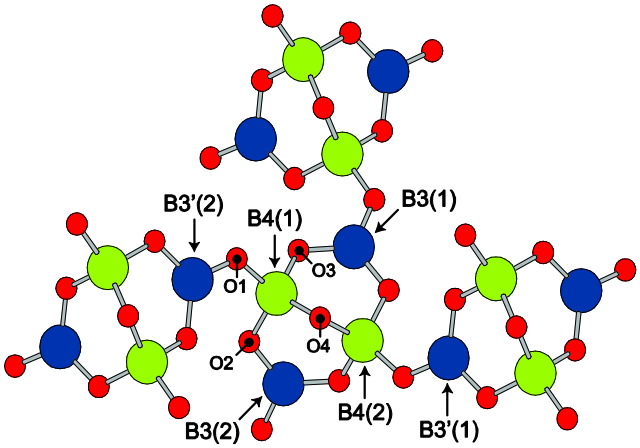

Fig. 1 Schematic representation of the diborate units in the crystal structure of lithium diborate.[80] Three- and four-coordinated boron atoms are shown in blue and green, respectively, while oxygen atoms are red. The labelling of boron and oxygen atoms as used in Tables 1 and 5, respectively, is indicated.

The root-sum-squared dipolar coupling is defined (see eqns. 3 and 6 of Ref. [81]) as :

$$d_{\mathrm{rss}} = \sqrt{\rho \sum_{j \neq k} d_{jk}^2} \qquad (2)$$

where ρ is the probability that a boron nucleus is the ^{11}B isotope. For ρ = 1, corresponding to 100% ^{11}B enrichment, d_{rss} equals 1.613 and 1.818 kHz for the B3 and B4 sites, respectively (considering boron atoms out to 10 Å).

Table 1 Boron-boron distances[a] and corresponding ^{11}B-^{11}B dipolar coupling constants as determined for the crystal structure of lithium diborate[80]

Nuclei	Separation / Å	d_{jk} / Hz
B4(1)–B4(2)	2.36	−937
B3(1)–B4(1)	2.44	−848
B4(2)–B3(2)	2.44	−848
B3(1)–B4(2)	2.49	−801
B4(1)–B3(2)	2.49	−801
B3'(1)–B4(2)	2.50	−791
B4(1)–B3'(2)	2.50	−791
B3(1)–B3(2)	3.58	−269

[a] Bracketed numbers are used to differentiate between different boron atoms in the same superstructural diborate group (see Fig. 1). B4-B4 and B4-B3 distances up to 2.50 Å are listed, noting that each B3 has a B-O-B connectivity to a B4 in a different superstructural group and vice versa. The shortest B3-B3 distance is tabulated.

In this paper, experimental data is presented for lithium diborate samples with four different degrees of ^{11}B isotopic abundance (5%, 25%, 80% and 100%). Table 2 presents the probabilities of a B3 ^{11}B nucleus having 0, 1, 2, or 3 ^{11}B neighbours and a B4 ^{11}B nucleus having 0, 1, 2, 3, or 4 ^{11}B neighbours for these ^{11}B isotopic abundances. The reduced probability of ^{11}B-^{11}B dipolar coupling for less than 100% ^{11}B isotopic abundance is reflected in the √ρ scaling in eqn (2): For 5%, 25% and 80% (natural abundance) ^{11}B, the root-sum-squared dipolar couplings are reduced to 22% (ρ = 0.05), 50% (ρ = 0.25) and 89% (ρ = 0.80) of the values stated above.

Table 2 The probability of a three- and four- coordinate ^{11}B nucleus being connected (via B-O-B bonds) to a given number of ^{11}B nuclei[a]

^{11}B	Site	Zero	One	Two	Three	Four
5%	B3	85.7%	13.5%	0.7%	0.0%	
5%	B4	81.5%	17.1%	1.4%	0.0%	0.0%
25%	B3	42.2%	42.2%	14.1%	1.6%	
25%	B4	31.6%	42.2%	21.1%	4.7%	0.4%
80%	B3	0.8%	9.6%	38.4%	51.2%	
80%	B4	0.2%	2.6%	15.4%	41.0%	41.0%
100%	B3	-	-	-	100%	
100%	B4	-	-	-	-	100%

[a] Connectivity probabilities as for crystalline lithium diborate,[80] where each boron forms only B-O-B bonds to other boron atoms.

^{11}B MAS NMR spectra of lithium diborate

^{11}B (14.1 T) MAS (10 kHz) NMR spectra of the four polycrystalline lithium diborate samples with different degrees of ^{11}B isotopic abundance are compared in Fig. 2. The narrow lineshape at ~2 ppm and the second-order quadrupolar broadened site centred at ~14 ppm are assigned to the B4 and B3 sites, respectively, for which the quadrupolar parameters are C_{Q} = 0.5 MHz and η_{Q} = 0.5 (B4) and C_{Q} = 2.60 MHz and η_{Q} = 0.2 (B3).[82-83] Increasing ^{11}B isotopic abundance leads to a broadening of both resonances that is most evident for the B4 site that exhibits negligible second-order quadrupolar broadening. This ^{11}B isotopic abundance dependent broadening is a consequence of MAS not fully averaging to zero over one rotor period the evolution under multiple homonuclear dipolar couplings, with this being due to the non-commutation of the dipolar Hamiltonian with itself at different times[42] – this effect is well known in ^{1}H MAS NMR.[81,84-85] For the B4 peak at ~2 ppm, it is evident that there is not a smooth change in the linewidth upon increasing ^{11}B isotopic abundance, with the 5% and 25% vs. 80% and 100% linewidths being similar. We presume that this difference lies in the non-linear dependence of the local homonuclear coupling strength on the degree of ^{11}B isotopic enrichment/depletion: in the 5 and 25% samples, the probability of a B4 site having two or more direct ^{11}B neighbours is less than 30%, while it is close to or equal to 100% for the 80 and 100% samples (see Table 2).

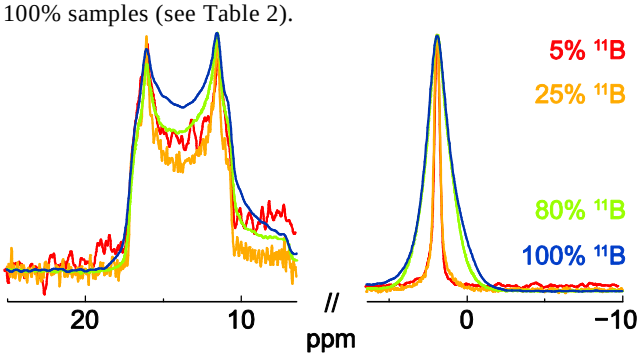

Fig. 2 ^{11}B (14.1 T) MAS (10 kHz) one-pulse spectra of samples of polycrystalline lithium diborate with varying degrees of ^{11}B isotopic abundance: 5 % (red), 25 % (orange), 80 % (natural abundance, green) and 100 % (blue). 32, 24, 8 and 16 transients were coadded using recycle delays of at least 60 s and a small flip angle. The ^{11}B probe background signal was removed by subtracting the spectrum acquired for an empty rotor with identical experimental settings. Spectra are normalised to the same vertical height.

^{11}B MAS NMR spin-echo dephasing curves for lithium diborate

This section considers ^{11}B MAS NMR spin-echo experiments performed at 14.1 T for polycrystalline lithium diborate. At this magnetic field, the B3 and B4 lineshapes are resolved (see Fig. 2), such that separate dephasing behaviour can be determined for the B3 and B4 sites. Fig. 3 compares the spin-echo dephasing behaviour at 20 kHz MAS for samples with three different degrees of ^{11}B isotopic abundance: 5%, 25% and 100%, while Fig. 4 compares the spin-echo dephasing behaviour of the 100% ^{11}B sample at MAS frequencies of 5, 10, 16, and 20 kHz.

Tables 3 and 4 present best fits of the spin-echo data in Figs. 3 and 4, respectively. Specifically, it is found (see Fig. S2 in the ESI) that the data is better fit to a bi-exponential function as compared to a mono-exponential function, i.e.,

$$S(\tau) = A(pe^{-\tau/T'_{2a}} + (1-p)e^{-\tau/T'_{2b}}) \quad (3)$$

where the parameter p corresponds to the proportion of the faster dephasing component ($T'_{2a} < T'_{2b}$). In order to quantify the observed trends in Figs. 3 & 4, Tables 3 and 4 list a composite $T'_{2[a+b]}$ that is defined as:

$$T'_{2[a+b]} = pT'_{2a} + (1-p)T'_{2b} \quad (4)$$

It is to be emphasised that a bi-exponential fit is a phenomenological description of the underlying coherent spin dynamics in the powder-averaged dipolar coupled multi-spin systems.[81] In this context, it is to be noted that quadrupolar T_1 relaxation is also expected to be multi-exponential in the solid state,[86] as discussed recently in the context of ^{17}O (I = 5/2) MAS exchange experiments.[87] We also note that bi-exponential relaxation (attributed to the central and satellite transitions) is observed in solution-state NMR of half-integer quadrupolar nuclei if there is restricted motion such that the motional correlation times are comparable to or larger than the inverse of the Larmor frequency.[88-89]

Table 3 Fit parameters[a] for spin-echo dephasing curves for polycrystalline lithium diborate with varying degrees of ^{11}B abundance (20 kHz MAS, see Fig. 3)

Site	^{11}B	A	p	T'_{2a} / ms	T'_{2b} / ms	$T'_{2[a+b]}$ / ms
B3	5%	1.04±0.02	0.23±0.02	0.6±0.1	92.7±6.6	71.5
B3	25%	0.98±0.01	0.11±0.02	7.8±2.1	51.8±1.6	47.0
B3	100%	1.02±0.01	0.20±0.05	2.2±0.7	12.1±0.7	10.1
B4	5%	1.02±0.02	0.29±0.04	1.9±0.6	37.2±4.2	27.0
B4	25%	1.03±0.01	0.35±0.02	1.6±0.1	19.0±0.7	12.9
B4	100%	1.07±0.02	0.90±0.07	1.9±0.2	12.4±9.9	3.0

[a] Fit to the bi-exponential function in eqn (3), with $T'_{2[a+b]}$ defined in eqn (4).

Considering the experimental spin-echo dephasing curves in Figs. 3 and 4 and the fits in Tables 3 and 4, the key observations are:

- The B3 (larger C_Q) site dephases more slowly than the B4 site (smaller C_Q) at all investigated MAS frequencies.
- Dephasing becomes faster for both B3 and B4 sites as the ^{11}B isotopic abundance increases.
- *Increasing* the *MAS frequency* leads to markedly *slower* dephasing for the *B3* site, while there is a much *less evident effect* for the *B4* site.

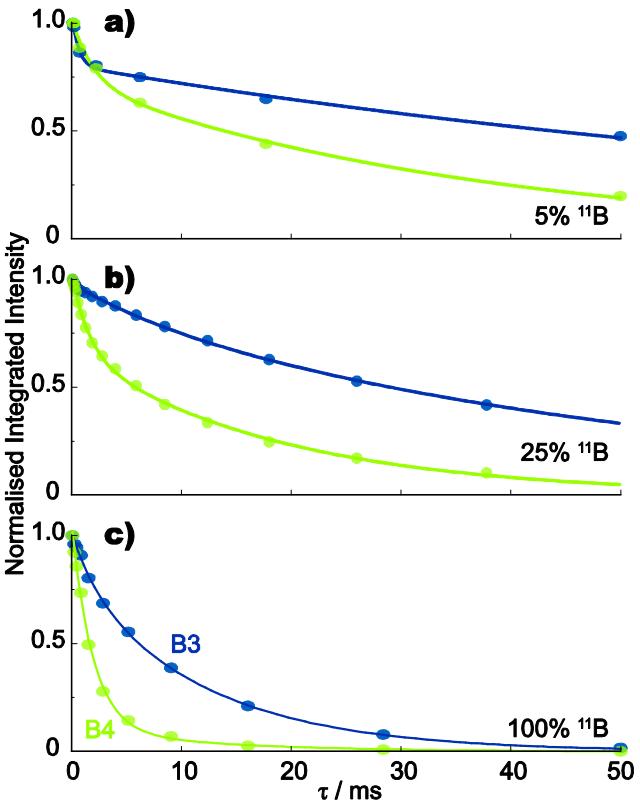

Fig. 3 ^{11}B (14.1 T) MAS (20 kHz) spin-echo (90° – τ/2 – 180° – τ/2 – t_{acq}) dephasing curves for samples of polycrystalline lithium diborate with varying degrees of ^{11}B isotopic abundance: (a) 5%, (b) 25%, and (c) 100%. 640 (5%), 384 (25%) and 96 (100%) transients were coadded for each spin-echo duration, τ. For both B3 (blue) and B4 (green) sites in all samples, the signal-to-noise ratio for this first point was at least 100:1. Best fits to the bi-exponential function in eqn (3) are shown as solid lines (see Table 3).

Table 4 Fit parameters[a] for spin-echo dephasing curves for polycrystalline lithium diborate with 100% ^{11}B abundance at varying MAS frequencies (see Fig. 4)

Site	MAS / kHz	A	p	T'_{2a} / ms	T'_{2b} / ms	$T'_{2[a+b]}$ / ms
B3	5	1.19±0.01	0.79±0.12	2.0±0.2	5.8±1.8	2.8
B3	10	1.04±0.01	0.53±0.19	3.8±0.8	10.3±2.1	6.9
B3	16	1.02±0.01	0.52±0.13	4.8±0.8	13.6±1.8	9.0
B3	20	1.02±0.01	0.20±0.02	2.2±0.7	12.1±0.7	10.1
B4	5	1.29±0.04	0.95±0.07	1.6±0.2	9.4±12.5	2.0
B4	10	1.11±0.02	0.88±0.10	2.2±0.3	11.4±8.7	3.3
B4	16	1.08±0.02	0.90±0.08	2.1±0.3	13.8±12.6	3.3
B4	20	1.07±0.02	0.90±0.07	1.9±0.2	12.4±9.9	3.0

[a] Fit to the bi-exponential function in eqn (3), with $T'_{2[a+b]}$ defined in eqn (4).

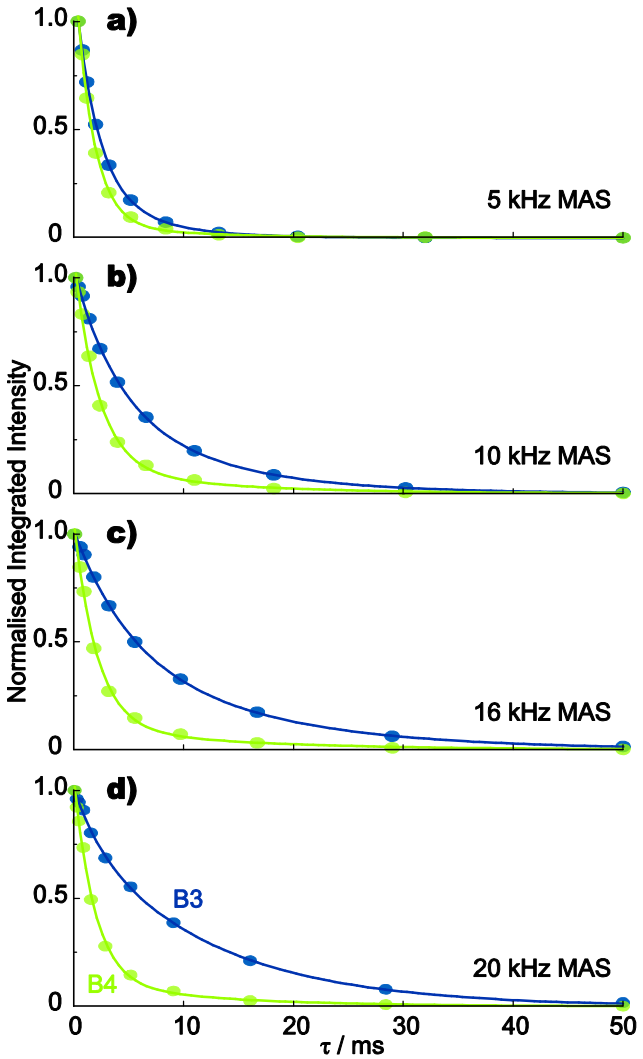

Fig. 4 ^{11}B (14.1 T) spin-echo dephasing curves for a sample of polycrystalline lithium diborate with 100% ^{11}B isotopic abundance, recorded at MAS frequencies of: (a) 5 kHz, (b) 10 kHz, (c) 16 kHz and (d) 20 kHz. 96 transients were coadded for each spin-echo duration, τ. For both B3 (blue) and B4 (green) sites in all samples, the signal-to-noise ratio for this first point was at least 200:1. Best fits to the bi-exponential function in eqn (3) are shown as solid lines (see Table 4).

Simulations of spin-echo dephasing

With the aim of understanding the experimentally observed phenomena, this section presents density-matrix simulations of spin-echo dephasing curves for, first, an isolated pair of dipolar-coupled ^{11}B nuclei and, second, an equilateral triangle arrangement of three dipolar-coupled ^{11}B nuclei. For the first case of two dipolar-coupled ^{11}B nuclei, the simulations show the effect of changing the MAS frequency for the spontaneous quadrupolar-driven recoupling mechanism. The three-spin simulations provide insight into the actual experimental situation for ^{11}B NMR of lithium diborate, where there is a competing effect of the non-commutation of multiple dipolar couplings.

Simulations of isolated pairs of dipolar-coupled ^{11}B nuclei

Fig. 5 presents simulated spin-echo dephasing curves at different MAS frequencies (from 5 to 20 kHz) for pairs of dipolar-coupled ^{11}B nuclei, where C_Q equals (a,c,e,g) 2.6 MHz and (b,d,f,h) 0.5 MHz, as in the case of the B3 and B4 sites in lithium diborate, respectively. Simulations are presented for the consideration of the quadrupolar interaction as (a-d) a first- or (e-h) a second-order perturbation of the Zeeman Hamiltonian. In (a,b) and (e,f), the quadrupolar tensors for the two spins were co-linear and perpendicular to the dipolar tensor (i.e., the internuclear vector), while in (c,d) and (g,h), the two quadupolar tensors were perpendicular with respect to each other and to the dipolar tensor – this is illustrated in Fig. 5i.

The following observations are apparent from a consideration of the simulated spin-echo dephasing curves in Fig. 5. Comparing the simulations for different MAS frequencies, faster dephasing is observed upon increasing the MAS frequency from 5 to 20 kHz. This is the opposite trend as compared to the above experimental behaviour – this is further considered below in the discussion of three-spin simulations. When comparing analagous simulations in Fig. 5, it is evident that faster dephasing is always observed for the B4 as compared to the B3 site. This latter observation is in agreement with the experimental behaviour. (In addition, Fig. S6 in the ESI shows that increasing the dipolar coupling, d_{jk}, leads to a faster dephasing.)

The simulated spin-echo dephasing curves in Fig. 5 are different for the case of first- and second-order quadrupolar interactions, with the differences being more pronounced for the larger-C_Q B3 site, where there is evident second-order quadrupolar broadening of the ^{11}B MAS NMR lineshape (see Fig. 2). Specifically, for the B3 simulations (compare Fig. 5a & 5e and 5c & 5g), the dephasing is noticeably slower when second-order quadrupolar effects are considered. In this context, we note that, for the case of first-order quadrupolar interactions, simulations including and omitting the spin-echo 180º pulse are *identical*. In other words, the spin-echo simulations are identical to simulations of the NMR signal due to the evolution of transverse magnetisation as created in a one-pulse experiment. Thus, for first-order quadrupolar interactions, the spin-echo simulations will exactly reproduce the trends observed by Edén and Frydman for the case of ^{11}B MAS lineshapes.[40] This observation is not surprising given that the first-order quadrupolar Hamiltonian is bilinear in the spin operator, ***I***, and is thus invariant under a 180º pulse. (The first-order quadrupolar coupling can be refocused in a quadrupolar echo experiment, $90_x - \tau - 90_y - \tau$.[90-91]) By contrast (as shown in Fig. S7), including the spin-echo 180º pulse has a very marked effect when second-order quadrupolar effects are considered, since otherwise the signal dephases rapidly under the influence of the anisotropic second-order quadrupolar broadening.

Given the difference between the B3 and B4 cases in Fig. 5, it is informative to investigate further by simulation the effect of the magnitude of the quadrupolar interaction on the rate of spin-echo dephasing. As a measure of the degree of spin-echo dephasing, we use here the simulated spin-echo intensity at τ = 0.55 ms, where the first point (corresponding to τ = 0 ms) in each simulated curve is normalised to unity. In this way,

faster dephasing corresponds to a smaller number, while no dephasing corresponds to a value of 1. Specifically, Fig. 6 plots the degree of spin-echo dephasing for different quadrupolar coupling strengths at a MAS frequency of 20 kHz. Note that when $\omega_Q^{PAS}/2\pi = C_Q = 0$, there is no dephasing since MAS perfectly refocuses, over a complete rotor period, the evolution due to a dipolar coupling alone for the case of a pair of nuclei.

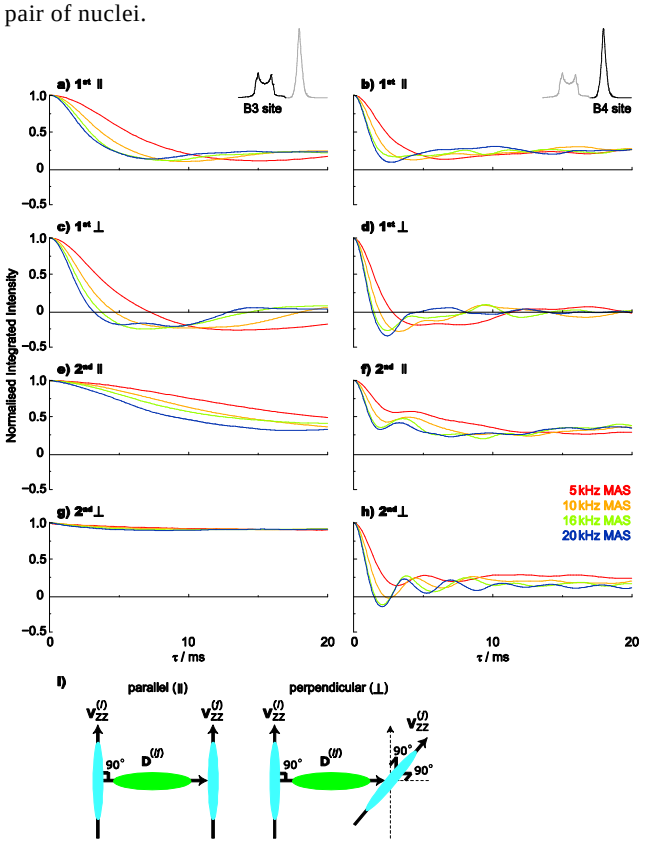

Fig. 5 Simulated (14.1 T) spin-echo dephasing curves for a pair of dipolar-coupled ($|d_{jk}|$ = 500 Hz) ^{11}B nuclei with the same isotropic chemical shift, where C_Q equals (a,c,e,g) 2.6 MHz (B3 site) and (b,d,f,h) 0.5 MHz (B4 site). Simulations were performed for MAS frequencies of 5 kHz (red), 10 kHz (orange), 16 kHz (green) and 20 kHz (blue) for evolution under (a-d) first- or (e-h) second-order quadrupolar interactions (η_Q = 0). In (a,b) and (e,f), the quadrupolar tensors for the two spins were co-linear and perpendicular to the dipolar tensor (i.e., the internuclear vector), while in (c,d) and (g,h), the two quadrupolar tensors were perpendicular with respect to each other and to the dipolar tensor. (i) An illustration of parallel and perpendicular quadrupolar tensor arrangements that shows the relative orientation of the largest magnitude component of the two electric field gradient tensors, $\mathbf{V}_{zz}$, with each other and with the dipolar coupling tensor, **D**. For the perpendicular arrangement, $\mathbf{V}_{zz}^{(j)}$ is out of the plane formed by $\mathbf{V}_{zz}^{(i)}$ and the dipolar coupling internuclear vector.

Fig. 6 shows four separate curves corresponding to the four cases in Fig. 5, i.e., first- or second-order quadrupolar interaction and parallel or perpendicular quadrupolar tensors. For all four curves, fastest dephasing is observed when $\omega_Q^{PAS}/2\pi$ is approximately equal to twice the MAS frequency. This corresponds to the same condition for observing maximum line broadening in MAS spectra noted by Edén and Frydman,[40] where the mechanism of "spontaneous quadrupolar-driven recoupling", i.e., the incomplete removal by MAS of the homonuclear dipolar coupling between two quadrupolar (I > 1/2) nuclei that arises from the non-commutation of the dipolar and quadrupolar couplings, is most efficient. The observation that both maximum MAS line broadening and maximum spin-echo dephasing occur when $\omega_Q^{PAS}/2\pi$ is approximately equal to twice the MAS frequency is unsurprising, since, firstly, the small value of the quadrupolar frequency for the observed dip corresponds to the case where second-order quadrupolar effects are negligible (note that the first- and second-order curves for the same arrangement of the quadrupolar tensors are overlayed in this region of the plot), and, secondly, it was noted above that spin-echo simulations are identical, for first-order quadrupolar interactions, to simulations of the NMR signal due to the evolution of transverse magnetisation as created in a one-pulse experiment. Slightly faster dephasing is observed at this position of most efficient "spontaneous quadrupolar-driven recoupling" for a perpendicular as compared to a parallel arrangement of the quadrupolar tensors – this trend is also apparent in Fig. 5 – with the same observation having been made by Edén and Frydman in the context of simulated MAS line broadening.[40] For $\omega_Q^{PAS}/2\pi$ > 225 kHz (C_Q > 900 kHz), the consideration of the quadrupolar interaction to second-order causes a slower dephasing as compared to the case of considering only the first-order quadrupolar interaction. Note that the plot in Fig. 6 only goes out to $\omega_Q^{PAS}/2\pi$ = 375 kHz (C_Q = 1.5 MHz); at larger quadrupolar frequencies, the difference becomes more evident (see the above discussion of the B3 case in Fig. 5).

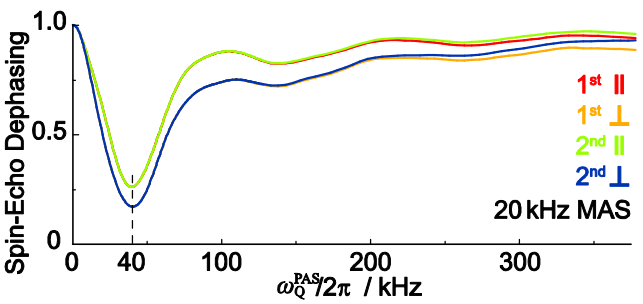

Fig. 6 The dependence of MAS (20 kHz, 14.1 T) spin-echo dephasing on the quadrupolar coupling strength, $\omega_Q^{PAS}/2\pi$ (equal to $C_Q/4$ for I = 3/2), simulated for a pair of dipolar-coupled ($|d_{jk}|$ = 500 Hz) ^{11}B nuclei with the same isotropic chemical shift. The degree of spin-echo dephasing is determined as the simulated spin-echo intensity at τ = 0.55 ms: As such, a smaller value corresponds to faster dephasing, and a value of unity corresponds to no dephasing. The four lines correspond to first-order quadrupolar interaction, parallel quadrupolar tensors (red); first-order quadrupolar interaction, perpendicular quadrupolar tensors (yellow); second-order quadrupolar interaction, parallel quadrupolar tensors (green); second-order quadrupolar interaction, perpendicular quadrupolar tensors (blue).

Fig. 7 shows how the extent of spin-echo dephasing depends on the MAS frequency in simulations of isolated pairs of dipolar-coupled ^{11}B nuclei for four different values of the quadrupolar frequency and the case of second-order quadrupolar interaction and perpendicular quadrupolar tensors. (Fig. S8 in the ESI presents analagous plots for the first-order limit and/or perpendicular quadrupolar tensors.) Note that $\omega_Q^{PAS}/2\pi$ = 130 kHz and 640 kHz correspond to C_Q = 0.5 MHz and 2.6 MHz, respectively, i.e., the C_Q values for

the B4 and B3 sites in lithium diborate. Considering the curves for $\omega_Q^{PAS}/2\pi$ = 60 kHz (red) and 130 kHz (orange), it is evident, as noted above, that fastest dephasing is observed when the MAS frequency is approximately equal to half the quadrupolar frequency, $\omega_Q^{PAS}/2\pi$. Remembering that the fastest MAS frequencies currently experimentally feasible are less than 100 kHz, different behaviour for these simulations of isolated spin pairs is observed for small and large quadrupolar interactions. For sites with small quadrupolar interactions, as the MAS frequency, ω_r, is increased, spin-echo dephasing becomes faster until $\omega_Q^{PAS} \sim 2\omega_r$, with the dephasing then becoming slower for further increases in the MAS frequency. For sites with large quadrupolar interactions, the isolated spin-pair simulations show minimal dependence of the spin-echo dephasing on the MAS frequency (for currently experimentally feasible MAS frequencies of less than 100 kHz).

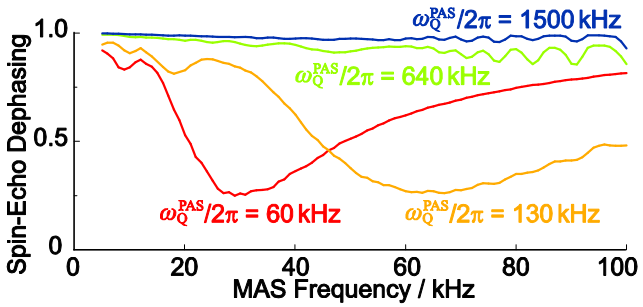

Fig. 7 The dependence of spin-echo dephasing on the MAS frequency, as simulated at 14.1 T for a pair of dipolar-coupled ($|d_{jk}|$ = 500 Hz) ^{11}B nuclei with the same isotropic chemical shift. Four different values of the quadrupolar frequency, $\omega_Q^{PAS}/2\pi$ (equals $C_Q/4$ for I = 3/2) are considered. The plots are for the case of second-order quadrupolar interaction and perpendicular quadrupolar tensors. The degree of spin-echo dephasing is determined as the simulated spin-echo intensity at τ = 0.55 ms.

Simulations of three dipolar-coupled ^{11}B nuclei

For spin-echo MAS NMR of homonuclear dipolar-coupled networks of spin I = 1/2 nuclei, it is known that the spin-echo linewidth decreases (i.e., slower dephasing) as the MAS frequency increases, e.g., see Fig. 2 of Ref.[81] and Fig. 5 of Ref.[16] for ^{1}H and ^{31}P spin-echo MAS NMR experiments, respectively. To achieve a realistic modelling of the experimental results, it is necessary to consider a model system that additionally takes into account the non-commutation of multiple dipolar couplings. Fig. 8, thus, presents simulated spin-echo dephasing curves for an equilateral triangle arrangement of three dipolar-coupled ^{11}B nuclei for MAS frequencies of 5 and 20 kHz. The simulations are for the case of second-order quadrupolar interactions, with the quadrupolar tensors for the three spins co-linear and perpendicular to the internuclear vectors that define the dipolar couplings.

A first observation is that faster dephasing is observed for the smaller-C_Q B4 site at both MAS frequencies, with the same observation having been made for the isolated spin-pair simulations presented above. Different behaviour as compared to the isolated spin-pair simulations is observed, however, when considering the effect of increasing the MAS frequency. For the larger-C_Q B3 site, slower dephasing is evident at 20 kHz MAS as compared to 5 kHz MAS. This is the opposite trend as compared to the isolated spin-pair simulations in Figs. 5 and 7, but is in agreement with the experimental results in Fig. 4 and Table 4. For the smaller-C_Q B4 site, the dephasing is similar at 20 kHz MAS as compared to 5 kHz MAS, with this distinction between the B3 and B4 site behaviour again matching the experimental results.

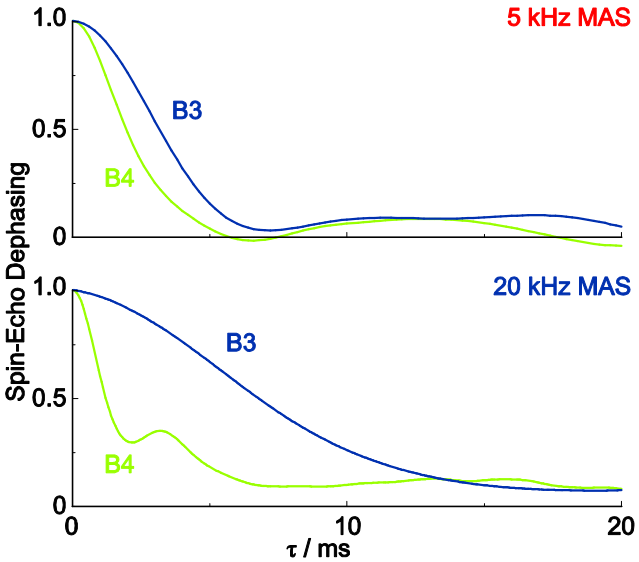

Fig. 8 Simulated (14.1 T) spin-echo dephasing curves for an equilateral triangle arrangement of three dipolar-coupled ($|d_{jk}|$ = 354 Hz for each pair of ^{11}B nuclei, such that d_{rss} = 500 Hz) ^{11}B nuclei with the same isotropic chemical shift, where C_Q equals 2.6 MHz (blue line, B3 site) or 0.5 MHz (green line, B4 site). Simulations were performed for MAS frequencies of 5 kHz (top) and 20 kHz (bottom) for evolution under second-order quadrupolar interactions (η_Q = 0), where the quadrupolar tensors for the three spins were co-linear and perpendicular to the plane of the dipolar tensors (i.e., the internuclear vectors).

Comparison of experiment and simulation

Experimentally, for ^{11}B spin-echo MAS NMR of polycrystalline lithium diborate with 100% ^{11}B abundance (Fig. 4 and Table 4), it is observed that increasing the MAS frequency leads to markedly slower dephasing for the B3 site, while there is a much less evident effect for the B4 site. While the isolated spin-pair simulations in Fig. 5 show faster dephasing as the MAS frequency is increased, the three-spin simulations in Fig. 8 show that slower dephasing is observed for the B3 site as the MAS frequency is increased, with the rate of dephasing for the B4 site varying little as the MAS frequency changes. The three-spin simulations are, thus, in agreement with experiment, i.e., as expected, the three-spin system is the more realistic model of the experimental situation.

There are thus two competing effects that explain the observed dependence of the spin-echo dephasing rate on the MAS frequency. On the one hand, there is the spontaneous quadrupolar-driven recoupling mechanism as described by Edén and Frydman[40-41], i.e., the incomplete removal by MAS of the homonuclear dipolar coupling between two quadrupolar (I > 1/2) nuclei that arises from the non-commutation of the

dipolar and quadrupolar couplings. As shown in the isolated spin-pair simulations, spontaneous quadrupolar-driven recoupling is associated with faster dephasing as the MAS frequency is decreased (for the case here where $\omega_Q^{PAS}/2\pi$ is bigger than the fastest MAS frequency). On the other hand, considering only homonuclear dipolar couplings, increasing the MAS frequency will lead to slower dephasing. The different experimental effect for the B3 and B4 sites in lithium diborate is explained by the different sensitivity of the spontaneous quadrupolar-driven recoupling mechanism to the MAS frequency for sites with different quadrupolar couplings. (Note that the root-sum-squared dipolar couplings, d_{rss}, are similar for the B3 (1.613 kHz) and B4 (1.818 kHz) sites.) Specifically, the simulations in Fig. 7 showed that there is a more pronounced effect associated with changing the MAS frequency (in the range 5 to 20 kHz) for the case of the B4 site with the smaller quadrupolar coupling. Thus, for the B4 site, where the experimental dephasing rate shows no marked dependence on the MAS frequency, it seems that the two competing effects cancel each other out. By comparison, for the B3 site, the influence of homonuclear dipolar couplings dominates, and slower experimental dephasing is observed as the MAS frequency is increased. This differing behaviour is reproduced in the three-spin simulations that take into account both the spontaneous quadrupolar-driven recoupling mechanism and the effect of non-commuting homonuclear dipolar couplings.

For ^{11}B spin-echo MAS NMR of crystalline lithium diborate, faster dephasing is always observed, for the considered MAS frequencies of 5 to 20 kHz, for the B4 site that has the smaller quadrupolar coupling. The same behaviour is observed in two- and three-spin simulations (compare the yellow and green lines in Fig. 7 that correspond to the C_Q values for the B4 and B3 sites, respectively, in lithium diborate, as well as Fig. 8) and can only be explained by the spontaneous quadrupolar-driven recoupling mechanism.

Experimentally, it is observed that ^{11}B spin-echo dephasing times increase as the percentage of ^{11}B decreases (see Fig. 3 and Table 3), as is to be expected due to the decrease in the effect of the homonuclear dipolar couplings, as quantified by the $\sqrt{\rho}$ dependence of the root-sum-squared dipolar couplings, d_{rss}, in eqn (2). It is to be noted that the longest dephasing times of ~12 ms for ^{23}Na (100% natural abundance) NMR of Na_2SO_4[58] and ^{27}Al (100% natural abundance) NMR of $CaAl_2O_7$[18] and $AlPO_4$ berlinite[92] reported in the literature are of the same duration as the longest dephasing time obtained from fits in this paper for lithium diborate at 100 % ^{11}B abundance sample (see Table 4). The ^{11}B spin-echo dephasing times determined here are three to four times shorter than the 30 to 50 ms values observed in spin-echo experiments for the spin I = 1/2 nucleus ^{31}P (100 % natural adundance, $\gamma(^{31}P)/\gamma(^{11}B)$ = 1.3) in inorganic phosphates for MAS frequencies between 10 and 20 kHz (see Table 4 in Ref,[10] Fig. 5 in Ref.[16] and Table 5 in Ref.[93]). Longer spin-echo dephasing times of 24 to 100 ms have been determined for ^{17}O spin-echo MAS NMR of partially ^{17}O-labelled glycine.HCl and uracil,[20] with these longer dephasing times being of the same magnitude as those obtained from fits in this paper for lithium diborate at 5 and 25% ^{11}B abundance sample (see Table 3).

First-principles NMR calculations of *J* couplings

There is a growing literature of examples where homonuclear J couplings are determined from spin-echo MAS NMR experiments for spin I = 1/2 nuclei such as ^{13}C, ^{15}N, ^{29}Si and ^{31}P.[10,16,47,61,93-98] In these cases, cosine modulation due to a J coupling leads to clear zero crossings (at $\tau = n/2J$, where n = 1, 3,… for a 90° – τ/2 – 180° – τ/2 – t_{acq} pulse sequence) allowing the J coupling constants to be determined to a high accuracy. While there is still significant signal intensity for the B3 site at a spin-echo duration of 166.6 ms for the ^{11}B MAS NMR spin-echo data in Fig. S2 of the ESI for polycrystalline lithium diborate with 25% ^{11}B isotopic abundance, no zero crossing is detectable. In the context of this observation, calculations of NMR parameters provide valuable insight in combination with experiment, e.g., for J couplings[99-102] as well as ^{11}B chemical shift and electric field gradient tensors.[103-104] This section presents first-principles calculations of the $^2J_{BB}$ couplings in lithium diborate.

First-principles calculations of the $^2J_{BB}$ couplings in lithium diborate were performed as described in Refs.[76,105] using the CASTEP software package, which implements density functional theory using a plane-wave basis set and the pseudopotential approach, and is thus applicable to periodic systems. Specifically, Table 5 lists the $^2J_{11B\text{-}11B}$ isotropic couplings for the four B-O-B bonds formed by each B4 atom in the lithium diborate crystal structure (see Fig. 1). As presented in the ESI, the calculations also determine the four separate contributions (Fermi contact, spin dipolar, paramagnetic orbital and diamagnetic orbital: the Fermi contact term is found to be the dominant term) as well as the J anisotropy (< 2 Hz) and the orientation of the J tensor with respect to the internuclear vector that defines the dipolar coupling (for B4-O-B3 J couplings, the largest principal component is found to be close (within 3°) to perpendicular to the internuclear vector). The ESI also presents calculated $^1J_{11B\text{-}17O}$ couplings that should be experimentally measurable in a ^{17}O-labelled sample, noting that the $^1J_{31P\text{-}17O}$ coupling in OPPh3 has been determined experimentally.[106-107]

The calculated isotropic $^2J_{11B\text{-}11B}$ couplings range from 1.0 to 2.7 Hz for the three distinct B4-O-B3 linkages between diborate units to 0.1 Hz for the coupling between two tetrahedral B sites (B4-O-B4). Further calculations (see ESI) have confirmed that these small $^2J_{11B\text{-}11B}$ are common to other boron-oxygen structural units: the coupling between the two trigonal B atoms in lithium metaborate is 3.2 Hz and the B3-O-B4 couplings in lithium triborate range from 1.2 to 1.9 Hz. Importantly, Fig. 9 reveals a strong correlation between the $^2J_{11B\text{-}11B}$ isotropic couplings and the B-O-B angle (Fig. 9a) and a weaker yet still evident correlation with the B-B distance (Fig. 9b), namely the J coupling increases as the B-O-B angle increases from a tetrahedral towards a linear arrangement (with a concomitant increase in the B-B distance). A similar trend for calculated J couplings has been observed for $^2J_{29Si\text{-}29Si}$ and $^2J_{31P\text{-}31P}$ couplings with respect to the Si-O-Si (see Fig. 5a of Ref.[98] and Fig. 2b of Ref.[108]) and P-O-P (see Fig. 9 in

Ref.[93]) bond angle, respectively. Moreover, it is to be noted that the experimental observation of larger $^2J_{29Si\text{-}29Si}$ and $^2J_{31P\text{-}31P}$ couplings correspond to compounds exhibiting larger Si-O-Si (e.g., 3.6 to 8.0 Hz for angles between 139º and 150º in parawollastonite[98] and 6.3 to 23.5 Hz for angles between 137º and 173º in the zeolite Sigma-2[108]) and P-O-P (e.g., 9 to 30 Hz for angles between 139º to 157º in $(MoO_2)_2P_2O_7$, see Tables 4 & 5 in Ref.[93]) bond angles, as compared to the B-O-B bond angles that are in the range 109º to 126º for lithium diborate.

Table 5 Calculated $^2J_{11B\text{-}11B}$ couplings[a] for lithium diborate[b]

	∠B-O-B / °	*r* (B-B) / Å	$^2J_{11B\text{-}O\text{-}11B}$ / Hz
B4-O1-B3	126	2.50	2.65
B4-O3-B3	119	2.49	1.20
B4-O2-B3	116	2.44	0.95
B4-O4-B4	109	2.36	–0.07

[a] Note that only the magnitude and not the sign of a *J* coupling can be determined by the cosine modulation in the experimental spin-echo approach. [b] The four B-O-B bonds formed by each B4 atom are labelled as in Fig. 1.

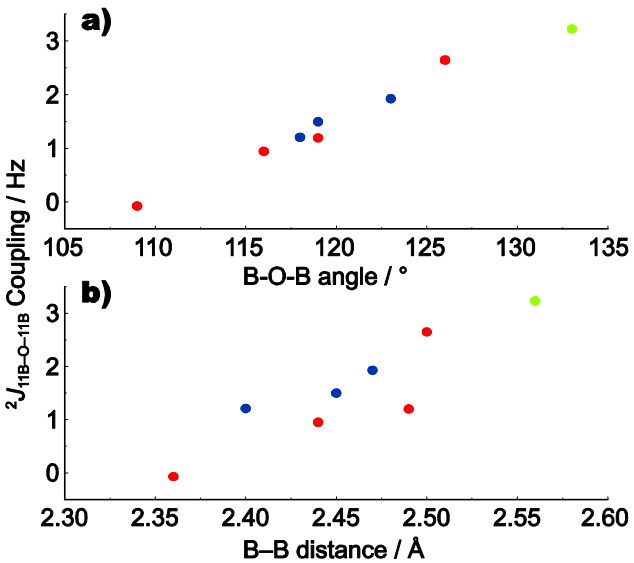

Fig. 9 The dependence of calculated $^2J_{BB}$ couplings on (a) the B-O-B angle and (b) the B-B distance for lithium diborate (red), lithium metaborate (green) and lithium triborate (blue).

The absence of an evident zero crossing due to a *J* modulation in the experimental spin-echo data for lithium diborate with 25% ^{11}B abundance in Fig. S2 (that goes out to a spin-echo duration of 250 ms) can be rationalised on the basis of the first-principles calculations shown in Table 5. Specifically, three different $^2J_{11B\text{-}11B}$ couplings of 2.65 Hz, 1.20 Hz and 0.95 Hz are calculated for the three distinct B3-O-B4 linkages. These small calculated couplings correspond to a first zero crossing ($\tau = 1/2J$) at 189 ms, 417 ms and 526 ms. Given the probabilities of a ^{11}B nucleus having one, two or three ^{11}B neighbours of 42%, 14% and 2% (see Table 2 for 25% ^{11}B abundance), it can be calculated that only 25% of all ^{11}B nuclei (42*0.33 + 14*0.67 + 2*1.00 = 25%) give rise to a spin-echo modulation characterised by the largest $^2J_{11B\text{-}11B}$ coupling (calculated as 2.65 Hz) for which a zero crossing would be expected for a spin-echo duration of 200 ms. As such (see Ref.[96] for an analagous discussion of ^{13}C spin-echo modulation for a cellulose sample with ~10% ^{13}C labelling), the observed spin-echo modulation will be dominated by the 75% of ^{11}B nuclei that do not exhibit a zero crossing at 200 ms.

Summary

To the best of our knowledge, there are no published examples of two-dimensional MAS homonuclear *J* correlation solid-state NMR experiments for quadrupolar nuclei. In this context, this paper has explored by experiment and simulation the factors affecting spin-echo dephasing in ^{11}B MAS NMR for the model compound, lithium diborate. The observed trends with respect to MAS frequency, ^{11}B isotopic abundance and C_Q are rationalised in terms of two phenomena. On the one hand, the reintroduction of the dipolar coupling due to the non-commutation of the dipolar and quadrupolar couplings (so-called spontaneous quadrupolar-driven recoupling, as described by Edén and Frydman[40-41]) is most efficient when the quadrupolar frequency, $\omega_Q^{PAS}/2\pi = 3C_Q/[4I\ (2I - 1)]$, is equal to twice the MAS frequency. On the other hand, the effect of multiple homonuclear dipolar couplings are progressively removed by faster MAS.

For the ^{11}B depleted samples, long spin-echo dephasing times are observed: for 25% ^{11}B, observable intensity is evident at spin-echo durations of ~200 ms. However, we were not able to observe a zero crossing due to a *J* modulation. This is consistent with first-principles calculations, where the three $^2J_{11B\text{-}11B}$ couplings in lithium diborate are calcuated as 0.95, 1.20 and 2.65 Hz. Interestingly, calculations for lithium diborate, lithium metaborate and lithium triborate reveal a clear trend whereby the calculated $^2J_{11B\text{-}11B}$ couplings increase from 0.95 to 3.23 Hz with increasing B-O-B bond angle (116º to 133º) and B-B distance (2.40 to 2.56 Å). A similar trend has been observed for the dependence on $^2J_{29Si\text{-}29Si}$ and $^2J_{31P\text{-}31P}$ couplings with respect to the Si-O-Si[98,108] and P-O-P[93] bond angle in silicates and phosphates; for silicates and phosphates, the bond angles are larger (>140º) and $^2J_{29Si\text{-}29Si}$ and $^2J_{31P\text{-}31P}$ couplings have been experimentally measured and utilised.

In conclusion, this paper has shown that, while ^{11}B spin-echo dephasing times can be favourably long, it is the small $^2J_{11B\text{-}11B}$ couplings that are a consequence of the small B-O-B bond angles observed in borates that are hampering the development of ^{11}B homonuclear *J* correlation solid-state NMR experiments. Such experiments may become feasible as ever faster MAS frequencies deliver longer spin-echo dephasing times.

Acknowledgements

Funding from EPSRC is acknowledged. NSB thanks the University of Warwick for a USA travel grant. Three Euler angle orientation sets were provided by Matthias Ernst (ETH Zürich). Anne-Christine Uldry is thanked for carrying out preliminary *J* coupling calculations. First-principles

calculations of *J* couplings were performed at the Oxford Supercomputer Centre.

Notes and references

[a]*Department of Physics, University of Warwick, Coventry, CV4 7AL,UK. E-mail: S.P.Brown@warwick.ac.uk*
[b]*Department of Materials, University of Oxford, Parks Road, Oxford OX1 3PH, UK.*
[c] *Physics Department, Coe College, Cedar Rapids, IA 52402, USA.*
[d] *School of Chemistry, University of St Andrews and EaStCHEM, St Andrews, Fife KY16 9ST, UK.*
[e] *Department of Chemistry, University of Durham, South Road, Durham, DH1 3LE, UK.*

† Electronic Supplementary Information (ESI) available: Additional experimental results: Powder X-ray diffraction and Raman spectra; comparing fits to a mono- and bi-exponential function; nutation spectra for the B3 and B4 sites in lithium diborate; spin-echo curves comparing the case where the *rf* amplitude was calibrated so as to give a 180° pulse duration of 25 μs for the B3 or B4 site; spin-echo curves comparing the case of a 4.2 μs as compared to a 25 μs 180° pulse duration; correlation coefficients for the fits of spin-echo dephasing curves. Additional simulation details and results: the effect of changing the dipolar coupling; the effect of including/ omitting the 180° pulse for first- and second-order quadrupolar interactions; the dependence of NMR spin-echo dephasing on the MAS frequency as in Fig. 7 for first-order quadrupolar interaction and/ or perpendicular quadrupolar tensors; a representative pnmrsim input file. Estimated magnitudes of second-order quadrupolar/dipolar and quadrupolar/CSA cross terms. Additional *J* coupling calculations: determination of the four separate contibutions to the calculated isotropic *J* couplings; definition and calculation of *J* anisotropy and relative orientation; calculation of $^{1}J_{BO}$; calculations for lithium metaborate and lithium triborate. See DOI: 10.1039/b000000x/

1. M. Baldus and B. H. Meier, *J. Magn. Reson. Ser. A*, 1996, **121**, 65.
2. A. S. D. Heindrichs, H. Geen, C. Giordani and J. J. Titman, *Chem. Phys. Lett.*, 2001, **335**, 89.
3. A. Lesage, M. Bardet and L. Emsley, *J. Am. Chem. Soc.*, 1999, **121**, 10987.
4. F. Fayon, D. Massiot, M. H. Levitt, J. J. Titman, D. H. Gregory, L. Duma, L. Emsley and S. P. Brown, *J. Chem. Phys.*, 2005, **122**, 194313.
5. S. Cadars, J. Sein, L. Duma, A. Lesage, T. N. Pham, J. H. Baltisberger, S. P. Brown and L. Emsley, *J. Magn. Reson.*, 2007, **188**, 24.
6. L. J. Mueller, D. W. Elliott, K. C. Kim, C. A. Reed and P. D. W. Boyd, *J. Am. Chem. Soc.*, 2002, **124**, 9360.
7. D. Lee, J. Struppe, D. W. Elliott, L. J. Mueller and J. J. Titman, *Phys. Chem. Chem. Phys.*, 2009, **11**, 3547.
8. H. Kono, T. Erata and M. Takai, *Macromolecules*, 2003, **36**, 5131.
9. F. Fayon, G. Le Saout, L. Emsley and D. Massiot, *Chem. Commun.*, 2002, 1702.
10. P. Guerry, M. E. Smith and S. P. Brown, *J. Am. Chem. Soc.*, 2009, **131**, 11861.
11. G. Grasso, T. M. de Swiet and J. J. Titman, *J. Phys. Chem. B*, 2002, **106**, 8676.
12. S. P. Brown, M. Perez-Torralba, D. Sanz, R. M. Claramunt and L. Emsley, *J. Am. Chem. Soc.*, 2002, **124**, 1152.
13. T. N. Pham, S. Masiero, G. Gottarelli and S. P. Brown, *J. Am. Chem. Soc.*, 2005, **127**, 16018.
14. S. Cadars, N. Mifsud, A. Lesage, J. D. Epping, N. Hedin, B. F. Chmelka and L. Emsley, *J. Phys. Chem. C*, 2008, **112**, 9145.
15. J. M. Griffin, J. R. Yates, A. J. Berry, S. Wimperis and S. E. Ashbrook, *J. Am. Chem. Soc.*, 2010, **132**, 15651.
16. D. Massiot, F. Fayon, M. Descamps, S. Cadars, P. Florian, V. Montouillout, N. Pellerin, J. Hiet, A. Rakhmatullin and C. Bessada, *C. R. Chim.*, 2010, **13**, 117.
17. S. Wi and L. Frydman, *J. Chem. Phys.*, 2000, **112**, 3248.
18. D. Iuga, C. Morais, Z. H. Gan, D. R. Neuville, L. Cormier and D. Massiot, *J. Am. Chem. Soc.*, 2005, **127**, 11540.
19. S. K. Lee, M. Deschamps, J. Hiet, D. Massiot and S. Y. Park, *J. Phys. Chem. B*, 2009, **113**, 5162.
20. I. Hung, A. C. Uldry, J. Becker-Baldus, A. L. Webber, A. Wong, M. E. Smith, S. A. Joyce, J. R. Yates, C. J. Pickard, R. Dupree and S. P. Brown, *J. Am. Chem. Soc.*, 2009, **131**, 1820.
21. S. E. Ashbrook and M. J. Duer, *Concepts Magn. Res. A*, 2006, **28A**, 183.
22. M. Edén, *Solid State Nucl. Magn. Reson.*, 2009, **36**, 1.
23. R. E. Youngman and J. W. Zwanziger, *J. Non-Cryst. Solids*, 1994, **168**, 293.
24. S. J. Hwang, C. Fernandez, J. P. Amoureux, J. Cho, S. W. Martin and M. Pruski, *Solid State Nucl. Magn. Reson.*, 1997, **8**, 109.
25. G. Ferlat, T. Charpentier, A. P. Seitsonen, A. Takada, M. Lazzeri, L. Cormier, G. Calas and F. Mauri, *Phys. Rev. Lett.*, 2008, **101**, 066504.
26. I. Hung, A. P. Howes, B. G. Parkinson, T. Anupold, A. Samoson, S. P. Brown, P. F. Harrison, D. Holland and R. Dupree, *J. Solid State Chem.*, 2009, **182**, 2402.
27. L. van Wullen and G. Schwering, *Solid State Nucl. Magn. Reson.*, 2002, **21**, 134.
28. L. S. Du and J. F. Stebbins, *J. Phys. Chem. B*, 2003, **107**, 10063.
29. P. M. Aguiar and S. Kroeker, *Solid State Nucl. Magn. Reson.*, 2005, **27**, 10.
30. M. Murakawi, T. Shimizu, M. Tansho, T. Akai and T. Yazawa, *Chem. Lett.*, 2010, **39**, 32.
31. B. G. Parkinson, D. Holland, M. E. Smith, A. P. Howes and C. R. Scales, *J. Non-Cryst. Solids*, 2005, **351**, 2425.
32. D. Caurant, O. Majerus, E. Fadel, A. Quintas, C. Gervais, T. Charpentier and D. Neuville, *J. Nucl. Mater.*, 2010, **396**, 94.
33. C. Gervais, F. Babonneau, J. Maquet, C. Bonhomme, D. Massiot, E. Framery and M. Vaultier, *Magn. Reson. Chem.*, 1998, **36**, 407.
34. C. Gervais, J. Maquet, F. Babonneau, C. Duriez, E. Framery, M. Vaultier, P. Florian and D. Massiot, *Chem. Mater.*, 2001, **13**, 1700.
35. M. Murakawi, T. Shimizu, M. Tansho, A. Vinu, K. Ariga, T. Mori and K. Takegoshi, *Solid State Nucl. Magn. Reson.*, 2007, **31**, 193.
36. D. L. Bryce, R. E. Wasylishen and M. Gee, *J. Phys. Chem. A*, 2001, **105**, 3633.
37. M. A. M. Forgeron, D. L. Bryce, R. E. Wasylishen and R. Rosler, *J. Phys. Chem. A*, 2003, **107**, 726.
38. S. E. Ashbrook, N. G. Dowell, I. Prokes and S. Wimperis, *J. Am. Chem. Soc.*, 2006, **128**, 6782.
39. A. C. Stowe, W. J. Shaw, J. C. Linehan, B. Schmid and T. Autrey, *Phys. Chem. Chem. Phys.*, 2007, **9**, 1831.
40. M. Edén and L. Frydman, *J. Chem. Phys.*, 2001, **114**, 4116.
41. M. Edén and L. Frydman, *J. Phys. Chem. B*, 2003, **107**, 14598.
42. M. M. Maricq and J. S. Waugh, *J. Chem. Phys.*, 1979, **70**, 3300.
43. M. H. Levitt, D. P. Raleigh, F. Creuzet and R. G. Griffin, *J. Chem. Phys.*, 1990, **92**, 6347.
44. Z. H. Gan and P. Robyr, *Mol. Phys.*, 1998, **95**, 1143.

45. G. Facey, D. Gusev, R. H. Morris, S. Macholl and G. Buntkowsky, *Phys. Chem. Chem. Phys.*, 2000, **2**, 935.
46. S. P. Brown and S. Wimperis, *J. Magn. Reson.*, 1997, **128**, 42.
47. A. Kubo and C. A. McDowell, *J. Chem. Phys.*, 1990, **92**, 7156.
48. R. Challoner, T. Nakai and C. A. McDowell, *J. Chem. Phys.*, 1991, **94**, 7038.
49. K. Eichele, G. Wu and R. E. Wasylishen, *J. Magn. Reson. Ser. A*, 1993, **101**, 157.
50. S. Dusold, E. Klaus, A. Sebald, M. Bak and N. C. Nielsen, *J. Am. Chem. Soc.*, 1997, **119**, 7121.
51. B. S. R. Sastry and F. A. Hummel, *J. Am. Ceram. Soc.*, 1958, **41**, 7.
52. R. K. Harris and E. D. Becker, *J. Magn. Reson.*, 2002, **156**, 323.
53. S. Hayashi and K. Hayamizu, *Bull. Chem. Soc. Jpn.*, 1989, **7**, 2429.
54. J. S. Frye and G. E. Maciel, *J. Magn. Reson.*, 1982, **48**, 125.
55. C. Huguenard, F. Taulelle, B. Knott and Z. H. Gan, *J. Magn. Reson.*, 2002, **156**, 131.
56. S. E. Ashbrook and S. Wimperis, *J. Magn. Reson.*, 2002, **156**, 269.
57. S. Antonijevic and G. Bodenhausen, *Angew. Chem.-Int. Edit.*, 2005, **44**, 2935.
58. H. T. Kwak, P. Srinivasan, J. Quine, D. Massiot and Z. H. Gan, *Chem. Phys. Lett.*, 2003, **376**, 75.
59. G. Pileio, Y. Guo, T. N. Pham, J. M. Griffin, M. H. Levitt and S. P. Brown, *J. Am. Chem. Soc.*, 2007, **129**, 10972.
60. G. Pileio, S. Mamone, G. Mollica, I. M. Montesinos, A. Gansmuller, M. Carravetta, S. P. Brown and M. H. Levitt, *Chem. Phys. Lett.*, 2008, **456**, 116.
61. T. N. Pham, J. M. Griffin, S. Masiero, S. Lena, G. Gottarelli, P. Hodgkinson, C. Fillip and S. P. Brown, *Phys. Chem. Chem. Phys.*, 2007, **9**, 3416.
62. P. Hodgkinson, *"pNMRsim: a general simulation program for large problems in solid-state NMR" URL: http://www.dur.ac.uk/paul.hodgkinson/pNMRsim/*.
63. P. Hodgkinson and L. Emsley, *Prog. Nucl. Magn. Reson. Spectrosc.*, 2000, **36**, 201.
64. M. Edén, *Concepts Magn. Res. A*, 2003, **17A**, 117.
65. M. Edén, *Concepts Magn. Res. A*, 2003, **18A**, 1.
66. M. Edén, *Concepts Magn. Res. A*, 2003, **18A**, 24.
67. J. McManus, R. Kemp-Harper and S. Wimperis, *Chem. Phys. Lett.*, 1999, **311**, 292.
68. S. E. Ashbrook, J. McManus, M. J. Thrippleton and S. Wimperis, *Prog. Nucl. Magn. Reson. Spectrosc.*, 2009, **55**, 160.
69. V. E. Zorin, M. Ernst, S. P. Brown and P. Hodgkinson, *J. Magn. Reson.*, 2008, **192**, 183.
70. S. K. Zaremba, *Ann. Mat. Pura. Appl.*, 1966, **73**, 293.
71. H. Conroy, *J. Chem. Phys.*, 1967, **47**, 5307.
72. V. B. Cheng, H. H. Suzukawa and M. Wolfsberg, *J. Chem. Phys.*, 1973, **59**, 3992.
73. C. J. Pickard and F. Mauri, *Phys. Rev. B*, 2001, **63**, 245101.
74. J. R. Yates, C. J. Pickard and F. Mauri, *Phys. Rev. B*, 2007, **76**, 024401.
75. www.gipaw.net.
76. S. Joyce, J. Yates, C. Pickard and F. Mauri, *J. Chem. Phys.*, 2007, **127**, 204107.
77. J. P. Perdew, K. Burke and M. Enzernhof, *Phys. Rev. Lett.*, 1999, **77**, 3865.
78. D. Vanderbilt, *Phys. Rev. B*, 1990, **41**, 7892.
79. N. Trouillier and J. L. Martins, *Phys. Rev. B*, 1991, **43**, 1993.
80. S. F. Radaev, L. A. Muradyan, L. F. Malakhova, Y. V. Burak and V. I. Simonov, *Kristallografiya*, 1989, **34**, 1400.
81. V. E. Zorin, S. P. Brown and P. Hodgkinson, *J. Chem. Phys.*, 2006, **125**, 144508.
82. M. R. Hansen, T. Vosegaard, H. J. Jakobsen and J. Skibsted, *J. Phys. Chem. A*, 2004, **108**, 586.
83. N. S. Barrow, S. E. Ashbrook, S. P. Brown and D. Holland, *Phys. Chem. Glasses-Eur. J. Glass Sci. Technol. Part B*, 2009, **50**, 201.
84. V. E. Zorin, S. P. Brown and P. Hodgkinson, *Mol. Phys.*, 2006, **104**, 293.
85. S. P. Brown, *Prog. Nucl. Magn. Reson. Spectrosc.*, 2007, **50**, 199.
86. E. R. Andrew and D. P. Tunstall, *Proc. Phys. Soc.*, 1961, **1**, 11.
87. P. Hodgkinson and M. R. Hampson, *Solid State Nucl. Magn. Reson.*, 2006, **30**, 98.
88. G. Jaccard, S. Wimperis and G. Bodenhausen, *J. Chem. Phys.*, 1986, **85**, 6282.
89. S. P. Brown and S. Wimperis, *Chem. Phys. Lett.*, 1994, **224**, 508.
90. J. H. Davis, K. R. Jeffrey, M. Bloom, M. I. Valic and T. P. Higgs, *Chem. Phys. Lett.*, 1976, **42**, 390.
91. S. Antonijevic and S. Wimperis, *J. Magn. Reson.*, 2003, **164**, 343.
92. J. P. Amoureux and J. Trebosc, *J. Magn. Reson.*, 2006, **179**, 311.
93. S. E. Lister, A. Soleilhavoup, R. L. Withers, P. Hodgkinson and J. S. O. Evans, *Inorg. Chem.*, 2010, **49**, 2290.
94. G. Wu and R. E. Wasylishen, *Inorg. Chem.*, 1992, **31**, 145.
95. L. Duma, W. C. Lai, M. Carravetta, L. Emsley, S. P. Brown and M. H. Levitt, *ChemPhysChem*, 2004, **5**, 815.
96. S. P. Brown and L. Emsley, *J. Magn. Reson.*, 2004, **171**, 43.
97. W. C. Lai, N. McLean, A. Gansmuller, M. A. Verhoeven, G. C. Antonioli, M. Carravetta, L. Duma, P. H. M. Bovee-Geurts, O. G. Johannessen, H. J. M. de Groot, J. Lugtenburg, L. Emsley, S. P. Brown, R. C. D. Brown, W. J. DeGrip and M. H. Levitt, *J. Am. Chem. Soc.*, 2006, **128**, 3878.
98. P. Florian, F. Fayon and D. Massiot, *J. Phys. Chem. C*, 2009, **113**, 2562.
99. J. Vaara, J. Jokisaari, R. E. Wasylishen and D. L. Bryce, *Prog. Nucl. Magn. Reson. Spectrosc.*, 2002, **41**, 233.
100. J. R. Yates, *Magn. Reson. Chem.*, 2010, **48**, S23.
101. D. L. Bryce, *Magn. Reson. Chem.*, 2010, **48**, S64.
102. C. Bonhomme, C. Gervais, C. Coelho, F. Pourpoint, T. Azais, L. Bonhomme-Coury, F. Babonneau, G. Jacob, M. Ferrari, D. Canet, J. R. Yates, C. J. Pickard, S. A. Joyce, F. Mauri and D. Massiot, *Magn. Reson. Chem.*, 2010, **48**, S86.
103. S. Sen, *Molec. Simul.*, 2008, **34**, 1115.
104. J. W. E. Weiss and D. L. Bryce, *J. Phys. Chem. A*, 2010, **114**, 5119.
105. S. A. Joyce, J. R. Yates, C. J. Pickard and S. P. Brown, *J. Am. Chem. Soc.*, 2008, **130**, 12663.
106. D. L. Bryce, K. Eichele and R. E. Wasylishen, *Inorg. Chem.*, 2003, **42**, 5085.
107. I. Hung, A. Wong, A. P. Howes, T. Anupold, J. Past, A. Samoson, X. Mo, G. Wu, M. E. Smith, S. P. Brown and R. Dupree, *J. Magn. Reson.*, 2007, **188**, 246.
108. S. Cadars, D. H. Brouwer and B. F. Chmelka, *Phys. Chem. Chem. Phys.*, 2009, **11**, 1825.